Nanoscale

PAPER

View Article Online
View Journal | View Issue

Cite this: *Nanoscale*, 2023, **15**, 5036

Single-site bipyridine cobalt complexes covalently embedded into graphitic carbon nitride with excellent photocatalytic activity and selectivity towards CO_2 reduction†

Jiajia Wei,[a] Xing Chen,[b] Chenying Liu,[a] Qian Zhou,[a] Shufang Tian, *[a] Ke-Fan Wang[c] and Minghua Lu *[a]

A combination of a semiconductor-based photosensitizer with molecular catalysts *via* covalent bonds is an effective way to utilize solar energy to reduce CO_2 into value-added chemicals with high efficiency and selectivity. In this study, 2,2′-bpy-5,5′-dialdehyde functioned as organic ligands and were embedded into the skeleton of g-CN through imine bonds *via* thermal copolymerization. The introduction of 2,2′-bpy can not only chelate with earth-abundant Co as single-site catalytic centers but also can optimize the properties of original g-CN such as the enlarged specific surface area and extended visible light absorption range. The CO evolution rate of g-CN-bpy-Co can reach up to 106.3 μmol g^{-1} h^{-1} with a selectivity of 97% over proton reduction, which was 82-fold than that of g-CN-Co. The different coordination environments and valence states of cobalt were also studied simultaneously and the results showed that Co(II) exhibited superior catalytic activity towards Co(III). Control experiments demonstrated that the covalent linkage between g-CN and Co-2,2′-bpy plays a vital role in photocatalytic activity and selectivity. Besides, the CO generation rate demonstrated linear growth upon visible light irradiation up to 72 h and preferable recyclability. This research provides a new facile way to fabricate low-priced photocatalysts with high activity and selectivity and bridge homogeneous and heterogeneous catalysis.

Received 23rd December 2022,
Accepted 30th January 2023

DOI: 10.1039/d2nr07202e

rsc.li/nanoscale

Introduction

Photocatalytic CO_2 reduction is an effective way to utilize solar energy to convert greenhouse CO_2 into value-added chemicals, which can not only relieve the energy shortage but also be conducive to alleviating the environmental pressure.[1–6] However, the sluggish kinetics of the CO_2 reduction process and varied reduction products due to the proton-assistant multi-electron transfer limit their practical applications. Thus, the design and fabrication of cheap, stable photocatalysts with high activity and selectivity is the key to CO_2 reduction.[7–12]

Molecular catalysts, especially noble metal (Rh, Re, and Ir) 2,2′-bipyridine complexes have been broadly studied as photocatalysts for CO_2 reduction not only due to their excellent catalytic activity and selectivity but also because of their adjustable metal ions and ligand structures.[13–20] As homogeneous catalysts, they always suffer from the limited photostability, tend to dimerize and further deactivate under illumination conditions. Besides, the difficulty of the recovery of molecular catalysts also hinders their practical applications. To solve the above obstacles, molecular catalyst heterogenization has proved to be a feasible strategy that can bridge the excellent catalytic performance of molecular catalysts and the robustness and recyclability of heterogeneous catalysts.[21,22] In general, molecular catalysts are still apt to leach from the support to the solution under long-term conditions if the two are combined by non-covalent attachment. Therefore, the confinement of molecular catalysts into MOFs or COFs is an appealing strategy as their stability and recyclability would obviously be enhanced, and the porosity of MOFs or COFs would contribute to rapid CO_2 diffusion and exposure of more catalytic sites.[23–27] However, the problem lies with extra photosensitizers, most of which are ruthenium 2,2′-bpy molecular photosensitizers, need to be added because the majority of MOFs or COFs lack sufficient photosensitivity to generate adequate electrons to reduce CO_2 under illuminations.[28,29] Hence,

[a]*Henan International Joint Laboratory of Medicinal Plants Utilization, College of Chemistry and Chemical Engineering, Henan University, Kaifeng 475004, Henan, China. E-mail: tianshufang@henu.edu.cn*
[b]*Key Laboratory for Special Functional Materials of Ministry of Education, Henan University, Kaifeng 475004, China*
[c]*Henan Key Laboratory of Photovoltaic Materials, Henan University, Kaifeng 475004, China*

† Electronic supplementary information (ESI) available. See DOI: https://doi.org/10.1039/d2nr07202e

the optimal approach is to couple molecular catalysts with semiconductors *via* covalent connections to fabricate the function-integrated heterogeneous photocatalysts and the resultant composite would facilitate rapid separation of the photo-generated electrons and holes and then photo-induced electrons migrate from the photosensitizer to molecular catalysts units, further heightening the photocatalytic performance.

Visible light-responsive graphitic carbon nitride (g-CN) as an organic polymeric semiconductor possesses a suitable bandgap (2.7 eV), easy preparation, and excellent thermal and chemical stability, which has been extensively investigated in photocatalytic CO_2 reduction, especially its two-dimensional planar structure is beneficial to more CO_2 absorbed and more catalytic centers exposed.[30–35] Several metal complexes based on Rh, Co have been reported in the hybrid form with g-CN through non-covalent or covalent interaction for photocatalytic CO_2 reduction and exhibited high turnover numbers and considerable robustness under long-term irradiation and covalent-linkage-boosted electron-transfer from g-CN to molecular catalytic centers.[36–41] Although the above strategy has made great progress towards CO_2 photo-reduction, there are still some aspects to be addressed. The first one is that the amino groups situated at the edges of g-CN are difficult to quantify and traditional liquid organic synthesis to link molecular catalysts with powder-state g-CN is time-consuming. The second is that pristine g-CN still suffers from the limited specific surface area and rapid recombination of photo-generated charge carriers, and the efficiency of the photo-induced electron transfers to the catalytic units is restricted. How to covalently link molecular metal complexes with g-CN and simultaneously optimize the physic-chemical properties of g-CN would dramatically promote CO_2 photoreduction efficiency?

Copolymerization with organic molecules bearing suitable functional groups such as amino, cyano, or aldehyde is a widely adopted approach to tuning the properties of g-CN.[42–47] A series of organic molecules have been covalently embedded into the skeleton of g-CN through facile one-pot thermal copolymerization and the visible-light absorption range, the specific surface area, and the conductivity of g-CN were apparently elevated to different degrees. To incorporate the dual-functional organic molecules, for example, 2,2′-bpy, which can not only regulate the properties of g-CN, the N atoms in 2,2′-bpy can concurrently coordinate with metal atoms as single-site catalytic centers is still less studied up to now.

Addressing this demand, herein, we choose 2,2′-bpy ligands modified with aldehyde groups in 5,5′ positions to copolymerize with urea to covalently integrate 2,2′-bpy into the matrix of g-CN through imine bonds, the resultant g-CN coordinates with the earth-abundant transition metal cobalt as the catalytic active centers. The experiments show that the obtained g-CN-bpy-Co can effectively reduce CO_2 to CO with high activity (106.3 μmol g^{-1} h^{-1}) and durability under visible-light irradiation. In addition, the control experiments demonstrate that the increased specific surface area, the extended light-absorption range, and the covalent bonds between the molecular catalyst and photosensitizer g-CN are the key factors responsible for superior CO_2 reduction performance than that of other hybrid means between g-CN and Co-2,2′-bpy.

Results and discussion

The thermal stability of 2,2′-bpy-5,5′-dialdehyde was first examined by thermogravimetric analysis (Fig. S1†), and the result showed that the first stage weight loss occurred at 150 °C. The temperature that urea melted to its liquid state usually occurs at 120 °C (ref. 48) and this liquid state will provide an environment to promote imine bonds formation and prevent 2,2′-bpy-5,5′-dialdehyde from decomposition or carbonization during the copolymerization process. In addition, this molten liquid medium will also promote a 2,2′-bpy skeleton well-distributed in the matrix of g-CN.

All g-CN-bpy samples were fabricated *via* one-pot thermal co-polymerization employing different mass ratios of urea and 2,2′-bpy-5,5′-dialdehyde as co-monomers. The photocatalysts g-CN-bpy-Co were synthesized by g-CN-bpy coordinated with different Co precursors *via* the hydrothermal method, as simulated in Scheme 1.

SEM images show that g-CN-*x* mg bpy (*x* = 0.5, 2, and 10) basically maintained a flaky nanostructure (Fig. 1b–d) as pure g-CN (Fig. 1a) except more mesoporous were generated along with the increasing content of 2,2′-bpy-5,5′-dialdehyde, matching well with the translucent porous nanosheets images investigated by TEM (Fig. 1f and g) in contrast with that of g-CN (Fig. 1e). It implies that the introduction of the ligands 2,2′-bpy as co-monomers indeed alters the condensation process of thermal polymerization. TEM mapping showed that the elements carbon, nitrogen, and cobalt are evenly distributed in the selected region, demonstrating that cobalt-2,2′-bpy was uniformly embedded into the skeleton of g-CN.

N_2 adsorption–desorption measurements were carried out to inspect the specific surface area and mesopore distribution. An obviously enhanced adsorption capacity was observed from the BET isotherms (Fig. 2a) and the specific surface area increased from 37 m^2 g^{-1} of g-CN to 100 m^2 g^{-1} of g-CN-2 mg-bpy. The isotherm for g-CN-2 mg bpy exhibited an apparent H1-type hysteresis loop at a relative pressure $P/P_0 > 0.8$, indicating the production of abundant mesopores, which is in accordance with the SEM and TEM results. The pore size distribution was mainly concentrated at 2.5 nm and 26 nm and the pore volume was dramatically promoted compared to that of pristine g-CN.

The XRD patterns of g-CN-*x* mg bpy show two distinct diffraction peaks at 13.2° and 27.4° were nearly the same as those in g-CN (Fig. 2b), which corresponded to (100) and (002) crystal planes, respectively, indicating that the crystal structures remained almost unchanged after copolymerization. The (100) crystal plane is attributed to the in-plane repeating motif of tri-*s*-triazine and the (002) plane originating from the interlayer stacking of the aromatic systems, which were gradually weakened and broadened; especially, the 2θ of the (002) plane became smaller meaning that the distances between two adja-

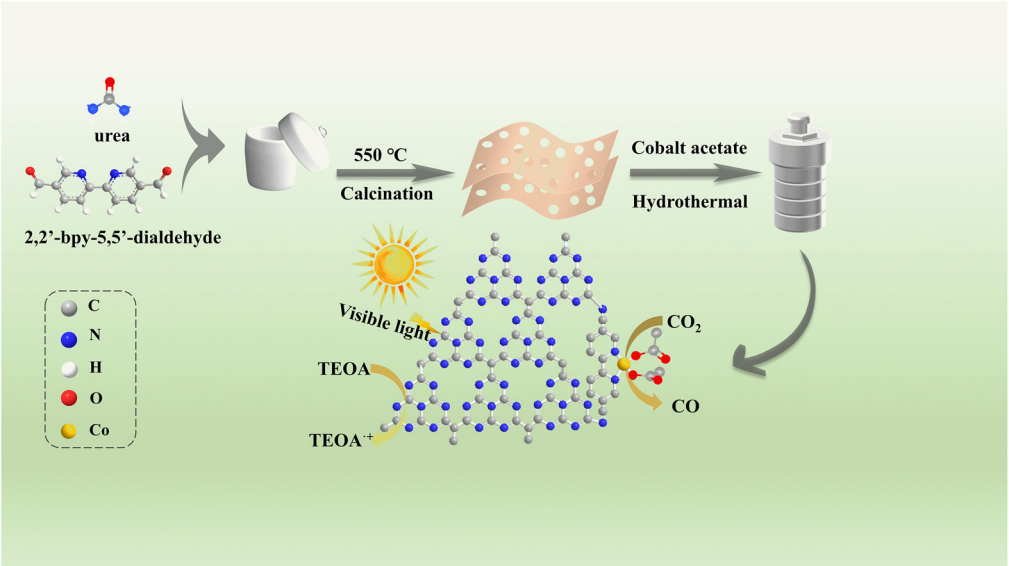

Scheme 1 Schematic illustration of the process of Co-2,2′-bpy covalently embedded into the framework of g-CN.

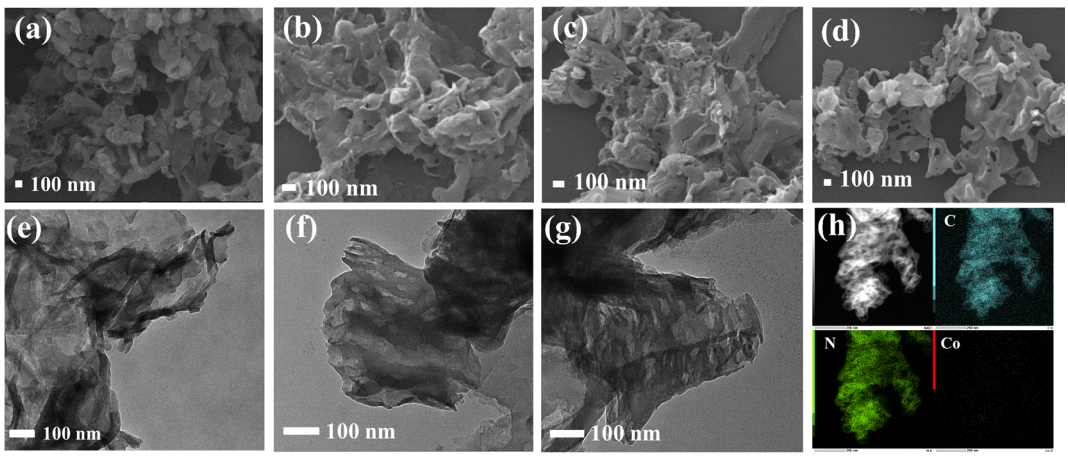

Fig. 1 SEM images of g-CN (a), g-CN-0.5 mg bpy (b), g-CN-2 mg bpy (c), g-CN-10 mg bpy (d). TEM images of g-CN (e), g-CN-2 mg bpy (f and g), and the elemental mapping of g-CN-2 mg bpy-Co (h).

cent layers of g-CN gradually enlarged along with the increase in the mass of 2,2′-bpy-5,5′-dialdehyde.

FT-IR spectra were further collected to reveal the chemical structures of g-CN-*x* mg bpy (Fig. 2c) and the results displayed identical characteristic absorption peaks as g-CN. The typical peak at 810 cm^{-1} is ascribed to the bending vibration of the triazine ring and the peaks around 1200–1720 cm^{-1} are assigned to the stretching vibrations of aromatic heptazine heterocycles, the broad peaks at 3000–3500 cm^{-1} are the contributions from the NH_2 groups located on the edges of the g-CN nanosheets. The characteristic peak at 1685 cm^{-1} belonging to the C=O of 2,2′-bpy-5,5′-dialdehyde disappeared and the formed imine bonds (C–C=N) ought to be located in the range of 1690–1640 cm^{-1} were not observed (Fig. S2†), perhaps due to the overlap with the peaks of heptazine heterocycles (N–C=N) of g-CN-2 mg bpy or were too weak to be seen.

The interfacial interaction and the surface chemical states were investigated by the XPS technique. As to g-CN, the binding energy of C 1s is dominantly situated at 288.12 eV, corresponding to the sp^2-hybridized C from N–C=N. While the C 1s spectra of g-CN-2 mg bpy were divided into two peaks, the position at 284.72 eV is attributed to sp^2-hybridized C=C that belonged to 2,2′-bpy,[34] the area of which increased with the content of 2,2′-bpy added (Fig. S3†), fully demonstrating that the ligands were kept intact after thermal polymerization (Fig. 2d). The N 1s spectrum of g-CN was deconvoluted into three peaks at 398.4, 400.1 and 401.3 eV (Fig. 2e), belonging to the sp^2-hybridized N (C–N=C) in the triazine rings, the sp^3-hybridized N ($N–C_3$) in the melem motif center, and NH_x groups in the g-CN framework, respectively. The peaks of sp^2-hybridized N (C–N=C) in g-CN-2 mg bpy shifted to the higher binding energy of about 0.24 eV compared with those of g-CN,

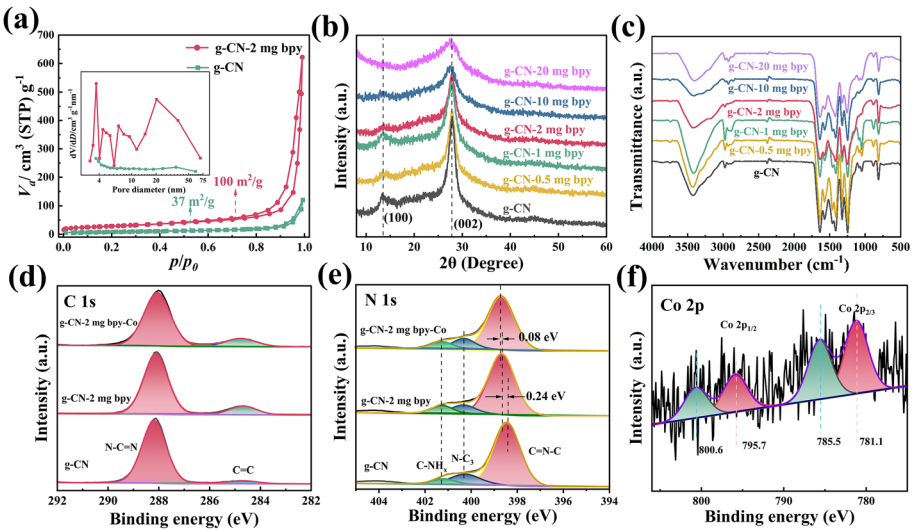

Fig. 2 N_2 adsorption–desorption isotherms and pore size distribution profile (inset) of the prepared samples of g-CN and g-CN-2 mg bpy (a), XRD patterns (b), FT-IR spectra (c) of g-CN and g-CN-*x* mg bpy (*x* = 0.5, 1, 2, 10, 20), and high-resolution XPS spectra C1s (d), N1s (e), Co2p (f) of g-CN, g-CN-2 mg bpy and g-CN-2 mg bpy-Co.

indicating that the electron cloud density in the heptazine ring decreased with the introduction of 2,2′-bpy, which sufficiently indicates the covalent interaction between g-CN and 2,2′-bpy. The elemental analysis outcomes gained from XPS are presented in Table S1;† the ratio of C/N increased accompanied by the improvement in the introduction amount of 2,2′-bpy. In addition, the content of different functional groups determined from the XPS results is also presented (Tables S2 and S3†). From the deconvoluted peaks of N 1s, the $-NH_x$ content was increased, which is consistent with the size of the g-CN-2 mg bpy nanosheets diminishing and the increases in the specific surface area. The $-NH_x$ groups suspending on the edges of the g-CN-2 mg bpy nanosheets correspondingly climbed. As to the sample g-CN-2 mg-bpy-Co, the binding energy of N (C–N=C) exhibited a weak shift from 398.7 to 398.8 eV, indicating the coordination interactions between N and Co. The loading content of Co was 0.1% measured by ICP and the fitting peak of $2p_{3/2}$ at 781.1 eV is the characteristic of Co^{2+} species.

The optical absorption properties of the g-CN and g-CN-*x* mg bpy were analyzed by UV-vis diffuse reflectance spectroscopy (Fig. 3a). The absorption threshold of g-CN is about 450 nm, while the absorption band edges of g-CN-*x* mg bpy are gradually red-shifted accompanying raising of the amount of 2,2′-bpy. The corresponding band gaps calculated are 2.79~2.55 eV according to the Tauc plots method (Fig. 3b), implying that the ligands have been incorporated into the lattice of g-CN connected by imine bonds, and the conjugated structure was expanded. Furthermore, the visible-light harvesting range of g-CN-*x* mg bpy was steadily widened, which is in line with the color changes of the samples (Fig. S4†).

EPR measurements were conducted to further study the electronic structure of the material. Compared with pure g-CN, the sample g-CN-2 mg bpy exhibited remarkably enhanced signals of the Lorentzian line with a g value of 2.0034 arising from the unpaired electrons in the CB of g-CN (Fig. 3c), demonstrating that more unpaired electrons were generated at the interface of 2,2′-bpy and g-CN. Especially under illumination conditions, the charge separation efficiency of g-CN-2 mg bpy was promoted more dramatically than that of g-CN. As to the sample g-CN-2 mg bpy-Co, the intensity of the signals was

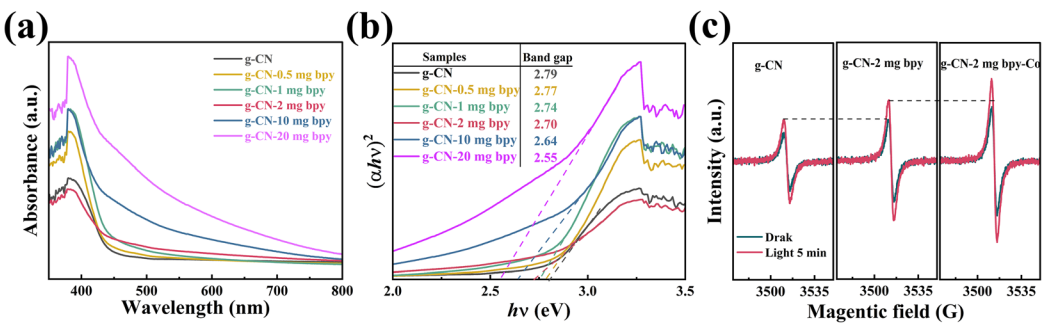

Fig. 3 UV-vis absorption spectra (a), plots of transformed Kubelka–Munk function corresponding band gap energies of g-CN and g-CN-*x* mg bpy (*x* = 0.5, 1, 2, 10, 20) (b), EPR signals of g-CN, g-CN-2 mg bpy and g-CN-2 mg bpy-Co (c).

further strengthened, indicating that the introduction of the catalytic center Co would be conducive to more unpaired electrons arising from the efficient separation of the generated electrons–holes.

Photocatalytic performance

The photocatalytic performances of the composites were evaluated from CO_2 reduction, which was carried out under mildly visible light irradiation employing a 5 W LED lamp as the lighting source (λ > 420 nm), acetonitrile as the reaction solvent, TEOA as the sacrificial electron donor and simultaneously providing protons. The main reduction product was CO along with a certain amount of H_2 generated as a byproduct. There was no CO produced when employing N_2 instead of CO_2, preliminarily demonstrating that CO originated from the reduction of CO_2.

The photoactivity of g-CN-Co and g-CN-*x* mg bpy Co are presented in Fig. 4a, CO and H_2 were selected as the major products to assess the activity and selectivity of all the samples. As can be seen, the CO evolution rate of the pristine g-CN with Co^{2+} loaded as the catalytic active centers was 1.3 μmol g^{-1} h^{-1}, accompanied by H_2 evolution at the rate of 1.1 μmol g^{-1} h^{-1} and the selectivity was 54%. When the ligands 2,2′-bpy are embedded into the matrix of g-CN and coordinate with Co^{2+} as single-site molecular catalysts, the CO generation rate was obviously enhanced and gradually heightened along with the increasement amount of 2,2′-bpy until 2 mg. The CO evolution rate can reach up to 106.3 μmol g^{-1} h^{-1} with a selectivity of 97% over H_2, which is more than 82 folds than that with g-CN-Co. The CO evolution rate descended when the amount of 2,2′-bpy exceeded 2 mg, maybe the introduction of too much ligand would destroy the conjugate structural integrity of g-CN and further weaken its light-harvesting ability.

A series of control experiments were also carried out to investigate the crucial factors responding to the excellent catalytic activity and selectivity (Fig. 4b). The complex Co-2,2′-bpy was first synthesized by refluxing $Co(CH_3COO)_2{\cdot}4H_2O$ with 2,2′-bpy-5,5′-dialdehyde in ethanol and then mixed with g-CN to form a hybrid through non-covalent physical grinding. The CO evolution rate exhibited certain optimization (1.6 μmol g^{-1} h^{-1}) with a selectivity of 47% over H_2, illustrating that the covalent linkage between molecular catalysts and g-CN is essential. Subsequently, the complex Co-2,2′-bpy, and pristine g-CN were covalently connected by imine bonds by refluxing in ethanol. The CO generation rate improved to 11.2 μmol g^{-1} h^{-1} but the selectivity dropped to 15%, demonstrating that the complex Co-2,2′-bpy preferred to reduce the proton to H_2 when grafted onto the edges of g-CN by means of the post-synthetic modification.

The effects of different coordination environments, including different cobalt precursors (II) and valence states (III) on photocatalytic performance, were also examined. As can be seen in Fig. 4c, all cobalt (II) performed well in CO_2 reduction activity around 90 μmol g^{-1} h^{-1}, especially with excellent selectivity of 97% over H_2 evolution. When employing cobalt (III) as the catalytic centers, the CO generation rate presented a certain declination to 60 μmol g^{-1} h^{-1}, while still maintaining good selectivity towards proton reduction, illustrating that the cobalt (II) exhibited superior catalytic performance towards CO_2 reduction than cobalt (III), but the catalytic performance has little connection with the anions of cobalt precursors.

The long-term stability of g-CN-2 mg bpy-Co was also investigated (Fig. 4d). When the complex Co-2,2′-bpy was embedded

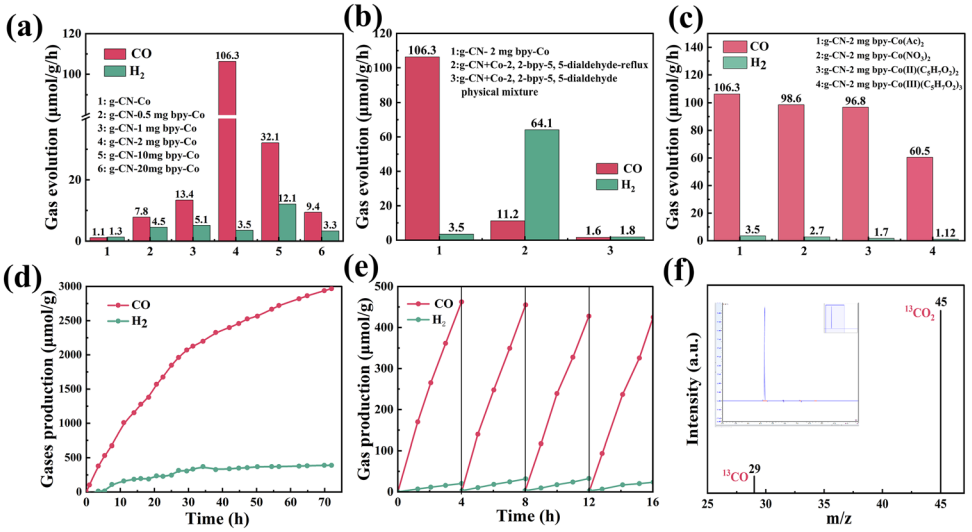

Fig. 4 Under visible light irradiation (λ > 420 nm), acetonitrile was used as the solvent, TEOA was used as the sacrificial agent, the CO and H_2 production rates of g-CN-Co and g-CN-*x* mg bpy Co samples (a), CO and H_2 production rate of g-CN-2 mg bpy-Co in comparison with the reflux of g-CN and bpy-Co at 80 °C in ethanol, the physical mixture of g-CN and Co-2,2′-bpy (b), CO and H_2 production rate of the diverse coordination environment covering various cobalt precursors (II) and valence states (III) (c), long-term durability of g-CN-2 mg bpy-Co sample during 72 h under visible light irradiation (d), recyclability evaluation of g-CN-2 mg bpy-Co under light condition for 4 cycles and each cycle lasted 4 h (e), the isotope labelling experiment to verify the origin of ^{13}CO (f).

into the skeleton of g-CN, they possessed superior robustness and their CO_2 reduction activity maintaining a nearly linear growth of up to 72 hours with the average CO evolution of 41.2 μmol g^{-1} h^{-1}. As a heterogeneous photocatalyst, the catalytic recyclability of g-CN-2 mg bpy-Co should also be evaluated (Fig. 4e), the experiments showed the CO production rate presented no noticeable declination after four consecutive cycles and each cycle lasted for 4 h, demonstrating its excellent robustness.

The isotope experiment was further conducted by employing $^{13}CO_2$ as the reactant to confirm the origin of the produced CO. The GC-MS results (Fig. 4f) showed that the peak situated at 4.3 min was attributed to m/z = 29 and assigned to ^{13}CO, implying that the CO indeed came from the CO_2 reduction, not from the decomposition of other components.

Lastly, the photocatalyst was recovered when the reaction was completed and characterized by FT-IR, XRD, SEM, and TEM (Fig. S5†). The results indicated that the morphology of the recovered photocatalysts was kept intact, and their chemical and crystal structures were also retained after long-term irradiation, suggesting the excellent stability of g-CN-2 mg bpy-Co.

Structure–activity relationship and mechanism discussion

Based on the above catalyst characterizations, the excellent photocatalytic CO_2 reduction activity and selectivity can be ascribed to the following factors. The covalent combination of 2,2′-bpy-5,5′-dialdehyde with g-CN *via* thermal copolymerization not only provided coordination sites for Co ions but also enlarged the specific surface area and extended the visible-light absorption range of g-CN. The inflated specific surface area of g-CN-2 mg bpy-Co is conducive to the adsorption of CO_2 molecules on its surface and exposure to more catalytic active centers. Simultaneously, the enhanced light harvesting ability increases the utilization and conversion of solar energy to chemical energy.

The migration and separation efficiency of the photo-generated electron–hole pairs is another crucial factor affecting photocatalytic performance. The combination of the electrons and holes was greatly inhibited due to the diminished thickness of the g-CN-2 mg bpy-Co nanosheets. The covalent imine bonds facilitated the electrons transferred from photosensitizer g-CN parts to the complex Co-2,2′-bpy, which can be confirmed by the steady-state and time-resolved photoluminescence spectra. The emission intensities of g-CN-2 mg bpy and g-CN-2 mg bpy-Co were significantly reduced in comparison with that of g-CN (Fig. 5a), indicating a lower combination rate of photo-generated charge carriers. The time-resolved photoluminescence spectra were also recorded to characterize the dynamic charger behaviors (Fig. 5b). The samples g-CN-bpy and g-CN-bpy-Co exhibited relatively fast decay kinetics and the average lifetimes calculated from double exponential function fitting were 4.46 and 3.95 ns, respectively, less than 6.35 ns of g-CN. The electron transfer rate (k_{ET}) calculated by employing the equation[48] from Table S4† was 9.6×10^7 s^{-1} between g-CN and the complex Co-2,2′-bpy, illustrating a fast spatial charge separation efficiency through imine bonds.

Electrochemical impedance spectroscopy (EIS) was performed to examine the interfacial properties of the photocata-

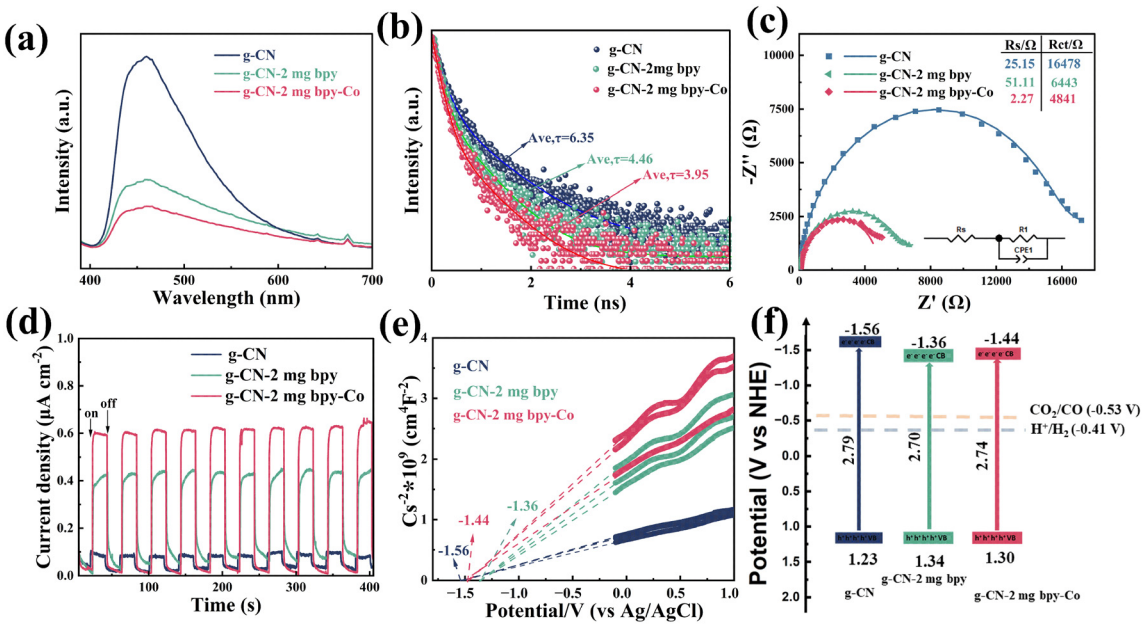

Fig. 5 Steady-state PL spectra (a), transient state PL spectra and fitting results (b), EIS Nyquist plots (c), photocurrent–potential curves (d), Mott–Schottky plots collected at different frequencies (1000 Hz, 1100 Hz, and 1200 Hz) (e), the electronic band structure of pure g-CN, g-CN-2 mg pby and g-CN-2 mg bpy-Co (f).

lysts. The results showed that the arc radii of g-CN-2 mg bpy and g-CN-2 mg bpy-Co were much smaller than that of pristine g-CN (Fig. 5c, Table S5†), indicating a lower resistance to a fast interfacial charge-carrier transfer of electrons when 2,2′-bpy was incorporated into the matrix of g-CN.

The charge separation efficiency was further studied by a photoelectrochemical test. The samples g-CN-2 mg bpy and g-CN-2 mg bpy-Co exhibited fast and steady photocurrent responses for ten repetitive cycles without significant decay (Fig. 5d), indicating the robustness of the samples under light irradiation. Moreover, the enhanced photocurrent density of g-CN-2 mg bpy and g-CN-2 mg bpy-Co proved that the interfaces constructed between 2,2′-bpy, and g-CN were favourable for charge separation and transfer compared with the photocurrent density of pure g-CN, which is consistence with the EIS analysis.

The band structure alignment was also analyzed based on UV-vis diffuse reflectance and electrochemical measurements, among which the flat potential was derived from Mott–Schottky plots (Fig. 5e). The calculated bandgap of g-CN-2 mg bpy was 2.7 eV, a trifle narrower than that of g-CN (2.79 eV), and the bandgap of g-CN-2 mg bpy-Co was slightly enlarged to 2.74 eV with the CB potential of −1.44 V *vs.* NHE, which is more negative than that of the required potential for reducing CO_2 to CO (−0.53 V, Fig. 5f).

Based on the results of the above study, a possible mechanism employing g-CN-bpy-Co for CO_2 photoreduction with high activity and selectivity (Table S6†) was proposed in Fig. 6. g-CN functioned as the photosensitizer absorbing visible light, especially, the light-harvesting ability of g-CN-bpy-Co was enhanced with the introduction of the ligand 2,2′-bpy. The electrons excited from the valence band of g-CN-bpy-Co to the conduction band under irradiation, the reduced size of the g-CN-bpy-Co nanosheets and lower resistance are conducive to inhibit electron–hole pairs recombination, promoting the electrons to migrate to 2,2′-bpy-Co part, which functioned as the catalytic center, and this process was accelerated by the covalent imine bonds that connected g-CN and 2,2′-bpy-Co. Meanwhile, the expanded specific surface area of g-CN-bpy-Co boosted the adsorption of more CO_2 molecules on its surface and more catalytic active centers Co were exposed, where CO_2 molecules chelated with Co and were activated. The stoichiometric transformation of CO_2 to CO is through the reaction: $CO_2 + H_2O \rightarrow CO + H_2 + O_2$. The process involves one electron participating to reduce CO_2 to $CO_2^{\bullet-}$, which is not easy at the reduction potential (−1.9 V) that is far higher than the conduction band of g-CN-bpy-Co (−1.44 V). As such, the proton-coupled two electrons reduction is more favored, resulting in CO_2 reduction to CO ($CO_2 + 2H^+ + 2e^- \rightarrow CO + H_2O$, −0.53 V). On the other hand, TEOA was employed as a sacrificial agent to capture the unreacted photo-induced holes to further promote the separation of electron–hole pairs and elevate the catalytic reduction activity. The excellent selectivity of g-CN-bpy-Co may be attributed to the uniformity of the coordination surrounding the catalytic center Co.

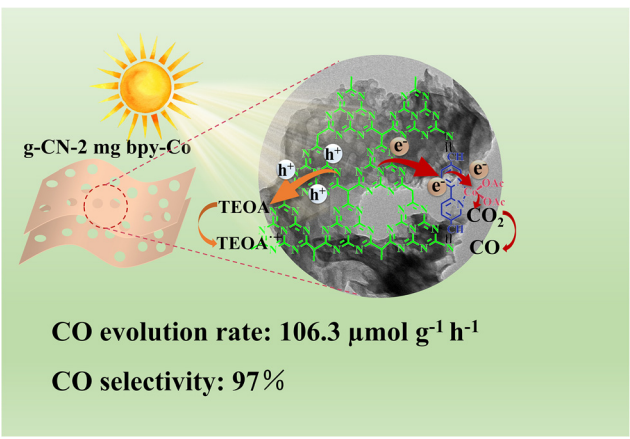

Fig. 6 The path of photo-induced electron transfer in the photocatalytic reduction of CO_2 to CO by g-CN-2 mg bpy-Co.

Conclusion

In summary, this paper describes the facile construction of function-integrated photocatalysts for CO_2 reduction. The ligand bipyridine dialdehyde was embedded into the framework of g-CN *via* covalent imine bonds through copolymerization, then, cobalt ions coordinated with the ligand and functioned as single-site catalytic centers. The heterogeneous nanocomposite not only exhibited excellent CO_2 reduction efficiency but also possessed outstanding long-term stability and multiple recyclabilities without apparent loss in the catalytic performance, benefitting from the optimized properties of g-CN as the enlarged specific surface area, the extended light-absorption range, and the covalent bonds between the molecular catalyst and photosensitizer g-CN.

Author contributions

S.T. and M.L. conceived the idea. J.W., X.C., and C.L. performed the experiments. Q.Z. and K.W. provided assistance in data analysis and characterization. All authors commented on the manuscript and contributed to the writing of the manuscript.

Conflicts of interest

The authors have no existing conflicts to declare.

Acknowledgements

This work was financially supported by the China Postdoctoral Science Foundation (2020M682275), and the National Natural Science Foundation of China (22004027).

References

1 T. Inoue, A. Fujishima, S. Konishi and K. Honda, *Nature*, 1979, **277**, 637–638.
2 J. Mao, K. Li and T. Peng, *Catal. Sci. Technol.*, 2013, **3**, 2481–2498.
3 S. C. Shit, I. Shown, R. Paul, K. H. Chen, J. Mondal and L. C. Chen, *Nanoscale*, 2020, **12**, 23301–23332.
4 J. Albero, Y. Peng and H. Garcia, *ACS Catal.*, 2020, **10**, 5734–5749.
5 M. Lu, M. Zhang, J. Liu, T.-Y. Yu, J.-N. Chang, L.-J. Shang, S.-L. Li and Y.-Q. Lan, *J. Am. Chem. Soc.*, 2022, **144**, 1861–1871.
6 M. Sayed, F. Xu, P. Kuang, J. Low, S. Wang, L. Zhang and J. Yu, *Nat. Commun.*, 2021, **12**, 4936.
7 J. Wang, R. T. Guo, Z. X. Bi, X. Chen, X. Hu and W. G. Pan, *Nanoscale*, 2022, **14**, 11512–11528.
8 Y.-F. Xu, M.-Z. Yang, B.-X. Chen, X.-D. Wang, H.-Y. Chen, D.-B. Kuang and C.-Y. Su, *J. Am. Chem. Soc.*, 2017, **139**, 5660–5663.
9 Y. Do, R. K. Chava, K. K. Mandari, N.-K. Park, H.-J. Ryu, M. W. Seo, D. Lee, T. S. Senthil and M. Kang, *Appl. Catal., B*, 2018, **237**, 895–910.
10 X. Li, Y. Sun, J. Xu, Y. Shao, J. Wu, X. Xu, Y. Pan, H. Ju, J. Zhu and Y. Xie, *Nat. Energy*, 2019, **4**, 690–699.
11 M. F. Kuehnel, K. L. Orchard, K. E. Dalle and E. Reisner, *J. Am. Chem. Soc.*, 2017, **139**, 7217–7223.
12 J. Y. Do, N. Son, R. K. Chava, K. K. Mandari, S. Pandey, V. Kumaravel, T. S. Senthil, S. W. Joo and M. Kang, *ACS Sustainable Chem. Eng.*, 2020, **8**, 18646–18660.
13 O. S. Wenger, *J. Am. Chem. Soc.*, 2018, **140**, 13522–13533.
14 A. J. Morris, G. J. Meyer and E. Fujita, *Acc. Chem. Res.*, 2009, **42**, 1983–1994.
15 A. V. Muller, M. R. Goncalves, L. D. Ramos, A. S. Polo and K. P. M. Frin, *Quim. Nova*, 2017, **40**, 200–213.
16 A. Kumar, P. Kumar, M. S. Aathira, D. P. Singh, B. Behera and S. L. Jain, *J. Ind. Eng. Chem.*, 2018, **61**, 381–387.
17 B. Gholamkhass, H. Mametsuka, K. Koike, T. Tanabe, M. Furue and O. Ishitani, *Inorg. Chem.*, 2005, **44**, 2326–2336.
18 Z. Guo, S. Cheng, C. Cometto, E. Anxolabehere-Mallart, S.-M. Ng, C.-C. Ko, G. Liu, L. Chen, M. Robert and T.-C. Lau, *J. Am. Chem. Soc.*, 2016, **138**, 9413–9416.
19 H. Takeda, K. Ohashi, A. Sekine and O. Ishitani, *J. Am. Chem. Soc.*, 2016, **138**, 4354–4357.
20 D. Hong, Y. Tsukakoshi, H. Kotani, T. Ishizuka and T. Kojima, *J. Am. Chem. Soc.*, 2017, **139**, 6538–6541.
21 N. Kim, I. Lee, Y. Choi and J. Ryu, *Nanoscale*, 2021, **13**, 20374–20386.
22 M. Lu, Q. Li, J. Liu, F.-M. Zhang, L. Zhang, J.-L. Wang, Z.-H. Kang and Y.-Q. Lan, *Appl. Catal., B*, 2019, **254**, 624–633.
23 S. Zhang, L. Li, S. Zhao, Z. Sun and J. Luo, *Inorg. Chem.*, 2015, **54**, 8375–8379.
24 D. Sun, Y. Gao, J. Fu, X. Zeng, Z. Chen and Z. Li, *Chem. Commun.*, 2015, **51**, 2645–2648.
25 X. Feng, Y. Pi, Y. Song, C. Brzezinski, Z. Xu, Z. Li and W. Lin, *J. Am. Chem. Soc.*, 2020, **142**, 690–695.
26 L. Zhao, Z. Zhao, Y. Li, X. Chu, Z. Li, Y. Qu, L. Bai and L. Jing, *Nanoscale*, 2020, **12**, 10010–10018.
27 S. Li, K. Ji, M. Zhang, C. He, J. Wang and Z. Li, *Nanoscale*, 2020, **12**, 9533–9540.
28 H. Fei, M. D. Sampson, Y. Lee, C. P. Kubiak and S. M. Cohen, *Inorg. Chem.*, 2015, **54**, 6821–6828.
29 X. Gao, B. Guo, C. Guo, Q. Meng, J. Liang and J. Liu, *ACS Appl. Mater. Interfaces*, 2020, **12**, 24059–24065.
30 X. Wang, K. Maeda, A. Thomas, K. Takanabe, G. Xin, J. M. Carlsson, K. Domen and M. Antonietti, *Nat. Mater.*, 2009, **8**, 76–80.
31 W.-J. Ong, L.-L. Tan, Y. H. Ng, S.-T. Yong and S.-P. Chai, *Chem. Rev.*, 2016, **116**, 7159–7329.
32 D. Xu, B. Cheng, W. Wang, C. Jiang and J. Yu, *Appl. Catal., B*, 2018, **231**, 368–380.
33 K. Chava, J. Do and M. Kang, *Appl. Catal., B*, 2019, **248**, 538–551.
34 H. Yu, R. Shi, Y. Zhao, T. Bian, Y. Zhao, C. Zhou, G. I. N. Waterhouse, L.-Z. Wu, C.-H. Tung and T. Zhang, *Adv. Mater.*, 2017, **29**, 1605148.
35 X. Niu, Y. Yi, X. Bai, J. Zhang, Z. Zhou, L. Chu, J. Yang and X. Li, *Nanoscale*, 2019, **11**, 4101–4107.
36 K. Maeda, K. Sekizawa and O. Ishitani, *Chem. Commun.*, 2013, **49**, 10127–10129.
37 R. Kuriki, H. Matsunaga, T. Nakashima, K. Wada, A. Yamakata, O. Ishitani and K. Maeda, *J. Am. Chem. Soc.*, 2016, **138**, 5159–5170.
38 Y. Zhang, J. Liu, Y. S. Kang and X. L. Zhang, *Nanoscale*, 2022, **14**, 11909–11922.
39 R. Kuriki and K. Maeda, *Phys. Chem. Chem. Phys.*, 2017, **19**, 4938–4950.
40 Y. Bo, C. Gao and Y. Xiong, *Nanoscale*, 2020, **12**, 12196–12209.
41 B. Ma, G. Chen, C. Fave, L. Chen, R. Kuriki, K. Maeda, O. Ishitani, T.-C. Lau, J. Bonin and M. Robert, *J. Am. Chem. Soc.*, 2020, **142**, 6188–6195.
42 J. Zhang, X. Chen, K. Takanabe, K. Maeda, K. Domen, J. D. Epping, X. Fu, M. Antonietti and X. Wang, *Angew. Chem., Int. Ed.*, 2010, **49**, 441–444.
43 M. H. Chan, R. S. Liu and M. Hsiao, *Nanoscale*, 2019, **11**, 14993–15003.
44 Z. Zhou, Y. Zhang, Y. Shen, S. Liu and Y. Zhang, *Chem. Soc. Rev.*, 2018, **47**, 2298–2321.
45 C. Yang, Y. Hou, G. Luo, J. Yu and S. Cao, *Nanoscale*, 2022, **14**, 11972–11978.
46 S. Tian, S. Chen, X. Ren, Y. Hu, H. Hu, J. Sun and F. Bai, *Nano Res.*, 2020, **13**, 2665–2672.
47 X. Zong, L. Niu, W. Jiang, Y. Yu, L. An, D. Qu, X. Wang and Z. Sun, *Appl. Catal., B*, 2021, **291**, 120099.
48 D. Qu, J. Liu, X. Miao, M. Han, H. Zhang, Z. Cui, S. Sun, Z. Kang, H. Fan and Z. Sun, *Appl. Catal., B*, 2018, **227**, 418–424.